ISSN 1392-3730/eISSN 1822-3605

VILNIUS TECH
Vilnius Gediminas Technical University

JOURNAL of CIVIL ENGINEERING and MANAGEMENT

2024
Volume 30
Issue 5
Pages 452–464
https://doi.org/10.3846/jcem.2024.21347

ANALYTICAL DISCUSSION ON APPLICABILITY OF FREQUENCY DOMAIN DECOMPOSITION METHOD TO SYSTEMS EXCITED BY AN IMPULSE FORCE

Kahori IIYAMA[1]✉, Hitoshi MORIKAWA[2], Ping-Yu CHEN[2], and Kimitoshi SAKAI[3]

[1] *Technical Research Institute, Kajima Corporation, Tokyo, Japan*
[2] *School of Environment and Society, Tokyo Institute of Technology, Tokyo, Japan*
[3] *Railway Technical Research Institute, Tokyo Japan*

Article History:
- received 29 September 2023
- accepted 24 March 2024

Abstract. This paper focuses on the use of vibration measurements for the purpose of cost-effective performance evaluation for the safety management and maintenance of Japan's social infrastructure like bridges. Since modal properties are often used to diagnose damage of structures by analysing their changes, various modal identification methods have been developed in the past few decades. Among these, the FDD method has still attractive attention because of its simplicity and practicality. It is also highly applicable to simultaneous observation at multiple points and even complex modes can be identified instantly. On the other hand, the applicability of this method to impact tests applied to evaluate the condition of structures has not been sufficiently discussed to date. In this study, we will clarify the applicability to impact tests by reconstructing the theoretical background of the FDD method. Furthermore, we will show from theory that when there is a correlation between inputs, higher-order singular values, which should be noted when applied to impact tests, will be affected. The conclusions obtained from the reconstruction of the theoretical background will be verified based on numerical experiments and actual observation records.

Keywords: frequency domain decomposition, modal identification, ambient vibration observation, impact force, cross-correlation inputs, bridge structure, numerical experiment.

✉Corresponding author. E-mail: *iiyamak@kajima.com*

1. Introduction

In Japan, social infrastructure, such as road structures built after high economic growth, is facing a renewal period. According to national statistics, approximately 43% of bridges managed by national and local authorities (400,000 bridges nationwide, excluding bridges with an unknown year of construction) are more than 50 years old. On the other hand, the number of engineers responsible for the maintenance and management of these structures is decreasing, and financial resources are becoming more difficult to secure, so it is an urgent issue to maintain and manage public structures efficiently. There is a need to develop technologies for easy and low-cost estimation of the condition of structures.

To estimate the physical state of structures in-service, methods focusing on local damage, such as image-based crack detection, are commonly used in recent years. On the other hand, methods using changes of dynamic parameters over time, which reflect global structural soundness, is also still useful. Actually, the modal properties estimated from vibration data can be utilized to estimate the stiffness reduction through optimization process (Ghannadi et al., 2023; Ghannadi & Kourehli, 2022). Qin et al. (2024) also employed FE model and applied the several model update algorithms to estimate the bridge structure, by using information on estimate modal properties. Recent development of data-driven model updating technique for structural and damage detection is introduced in the literature (Noori et al., 2024).

The dynamic property of a structure is identified mainly based on the vibration response obtained from microtremor measurements, seismic motion observations or impact tests. Among them, as the microtremors and the impact forces can be measured "at any time" without knowing the input properties, it would be very useful to develop

an identification technique that can deal with these in a unified manner.

Output-only modal identification based on the microtremor is mainly classified into time-domain-based techniques (Naira et al., 2006; Gul & Catbas, 2011; Mosavi et al., 2012; Chen et al., 2021), frequency-domain-based ones, and their mixture (Kang et al., 2021), various methods have been developed for both in recent decades. The time-domain based techniques have generally higher spectral estimation accuracy; however, their identification procedure tends to be more complex than the frequency-domain based ones. A representative method of the latter is the frequency domain decomposition (FDD) method (Brincker et al., 2000, 2001), followed by updating the mathematical processing for mode extraction (Zhang et al., 2005), improvement in spectral estimation methods (Rodrigues et al., 2004), development of damping identification technique (Danial et al., 2018), automation of identification procedure (Brincker et al., 2007), and so on.

These development of identification techniques using the FDD method has been progressing and its practicality has been improving. Bridges (Lee et al., 2006; Rodriguez-Suesca et al., 2022), building structures (Zhang et al., 2010; Van, 2016), and subsurface ground (Ermert et al., 2014; Poggi et al., 2014; Suzuki et al., 2022) are often the targets of mode identification by the FDD method. This technique is particularly attractive for modal identification of bridges and buildings because it can easily identify even higher-order modes by using multiple sensors with appropriate sensitivity. In addition, there are several methods to improve the estimation quality of the FDD method using stochastic approaches (Hizal, 2020; Hizal & Aktaş, 2021), Baysian based approaches (Au, 2011; Yan & Katafygiotis, 2015; Hizal & Turan, 2020), least squares method (Hizal, 2023a) or machine learning approaches (Qu et al., 2023).

Moreover, the input-output methods have also been discussed. Baysian approach technique has applied for known seismic response (Hizal, 2023b; Ni & Zhang, 2019), and quantitative evaluation of estimation accuracy is also discussed for known broadband input (Ng et al., 2023). The conventional FDD method assumes the white-noise input. However, the actual microtremor is not pure white noise in most cases. Then it is difficult to accurately separate the response characteristics of the target system from the characteristics of the input, depending on the target (Mostafavian et al., 2019). Pioldi et al. (2015, 2017a, 2017b) proposed a refined FDD method and applied it to a high damping building system for seismic loading, which are non-white inputs, and obtained the modal parameters with good accuracy. However, the refined FDD focuses on improving the accuracy of spectral estimation from time series and does not mention the relationship between input characteristics and identification results in the theory of the FDD method.

In this way, there are a lot of fruitful research to improved or extended modal identification technique. On the other hand, a motivation of this study is simple; It is to reveal the applicability of the FDD method to impact testing, which is conducted to diagnose the structural soundness. As impact force theoretically has property like white noise, their application to the FDD method does not seem sensibly problematic, but it is important to demonstrate this based on a theoretical background.

This study considers the applicability of the FDD method to impact testing from the theoretical background. Specifically, we reconstruct the theoretical background of his previous FDD work (Brincker et al., 2000, 2001), focusing on the influence of the input characteristics of the system, and discuss its effect on identification accuracy. Next, paying attention to the fact that mode identification uses peak picking, we focus on the case where there is a correlation between the inputs, which might be a factor that unintentionally affects the shapes of high-order singular values identified by the FDD method. In the case of ground motion input, for example, there is a strong correlation between the inputs because acceleration acts on the structure in the same phase as inertial force. The same applies to wind input. As mentioned above, although research has been conducted on methodologies to improve identification accuracy for seismic motion input, verification from FDD theory has not been conducted. We also discuss the identified singular values for the case that inputs have strong correlations, based on the theoretical background. Finally, these considerations will be verified through numerical experiments and observation records.

2. Theoretical background of frequency domain decomposition

Referring to the theoretical background of the conventional FDD method proposed by Brincker et al. (2000), the power spectral density matrix (PSD) of the vibrational system, which is a Hermitian matrix, is expressed as the shape of the singular value decomposition (SVD).

The relationship between the unknown l number of inputs $x_i(t)$ (i = 1, …, l) and m measured responses $y_i(t)$ (i = 1, …, m) can be expressed in the frequency domain (Bendat & Piersol, 1993) as:

$$\boldsymbol{G}_{yy}(\omega)=\boldsymbol{H}^{*}(\omega)\boldsymbol{G}_{xx}(\omega)\boldsymbol{H}^{T}(\omega), \tag{1}$$

where the superscripts * and T respectively represent the complex conjugate and transpose, $\boldsymbol{G}_{yy}(\omega)$ is the $m\times m$ PSD matrix of the responses (output), $\boldsymbol{G}_{xx}(\omega)$ is the $l\times l$ PSD matrix of the inputs, and $\boldsymbol{H}(\omega)$ is the $m\times l$ frequency response function (FRF) matrix. The FRF matrix can be expressed as a partial fraction, that is, in the pole/residue form as:

$$\boldsymbol{H}(\omega)=\sum_{k=1}^{n}\left[\frac{\boldsymbol{R}_k}{j\omega-\lambda_k}+\frac{\boldsymbol{R}_k^{*}}{j\omega-\lambda_k^{*}}\right], \tag{2}$$

where n is the number of modes, j is the imaginary number, and λ_k is the pole. $\boldsymbol{R}_k$ is the residue, and is expressed as:

$$\boldsymbol{R}_k=\boldsymbol{\phi}_k\boldsymbol{\gamma}_k^{T}, \tag{3}$$

where $\boldsymbol{\phi}_k$, $\boldsymbol{\lambda}_k$ are respectively the mode shape vector and modal participation vector. Supposing the input is white noise, i.e., $\boldsymbol{G}_{xx}(\omega)=\boldsymbol{\Gamma}$, the following equation can be obtained by substituting Eqn (2) into Eqn (1):

$$\boldsymbol{G}_{yy}(\omega)=\sum_{k=1}^{n}\left[\frac{\boldsymbol{A}_k}{j\omega-\lambda_k}+\frac{\boldsymbol{A}_k^*}{j\omega-\lambda_k^*}+\frac{\boldsymbol{A}_k^{*T}}{-j\omega-\lambda_k^*}+\frac{\boldsymbol{A}_k^T}{-j\omega-\lambda_k}\right], \tag{4}$$

where $\boldsymbol{A}_k$ is the k-th residue matrix of the output PSD, given by

$$\boldsymbol{A}_k=\sum_{s=1}^{N}\left\{\frac{\boldsymbol{R}_s}{-\lambda_k-\lambda_s}+\frac{\boldsymbol{R}_s^*}{-\lambda_k-\lambda_s^*}\right\}\boldsymbol{\Gamma}\boldsymbol{R}_k^T. \tag{5}$$

The pole is represented as $\lambda_k=-\sigma_k+j\omega_{dk}$, where ω_{dk} is the damped circular natural frequency. σ_k is the scalar, which is represented as the product of the k-th modal damping factor h_k and the circular natural frequency ω_k for the proportional damping system ($\sigma_k=h_k\omega_k$). Then, the second term in Eqn (5) becomes extremely dominant when $s=k$ for a system with small modal damping, and the k-th residual is proportional to the mode-shape vector. Replacing $\boldsymbol{\phi}_k^*$ with $\boldsymbol{\phi}_k$ does not change the essence,

$$\boldsymbol{A}_k\propto\boldsymbol{R}_k^*\boldsymbol{\Gamma}\boldsymbol{R}_k^T=\beta_k\boldsymbol{\phi}_k\boldsymbol{\phi}_k^H, \tag{6}$$

where superscript H denotes the complex conjugate and

$$\beta_k=\boldsymbol{\gamma}_k^H\boldsymbol{\Gamma}\boldsymbol{\gamma}_k.$$

At a certain frequency ω, only a limited number of modes contribute significantly. Let the set of modes be denoted as Sub(ω). Thus, in the case of a lightly damped structure, the response PSD can be written as Eqn (7) by using a constant $\hat{d}_k$:

$$\boldsymbol{G}_{yy}(\omega)\approx\sum_{k\in Sub(\omega)}\left[\frac{\hat{d}_k\boldsymbol{\phi}_k\boldsymbol{\phi}_k^H}{j\omega-\lambda_k}+\left(\frac{\hat{d}_k\boldsymbol{\phi}_k\boldsymbol{\phi}_k^H}{j\omega-\lambda_k}\right)^*\right]. \tag{7}$$

The detail of $\hat{d}_k$ will be revealed in Section 3.1, and its direct derivation is introduced in Appendix A. On the contrary, $\boldsymbol{G}_{yy}(\omega)$ can be decomposed through SVD because it is a Hermitian matrix:

$$\boldsymbol{G}_{yy}(\omega)=\boldsymbol{USU}^{\boldsymbol{H}}=\sum_l s_l(\omega)\boldsymbol{u}_l(\omega)\boldsymbol{u}_l^H(\omega), \tag{8}$$

where $\boldsymbol{U}$ is a unitary matrix holding the singular vectors $\boldsymbol{u}_l(\omega)$, and $\boldsymbol{S}$ is a diagonal matrix holding the scalar singular values $s_l(\omega)$ ($s_1>\ldots>s_m$). Calculating $\boldsymbol{G}_{yy}(\omega)$ for each discretized frequency ω_i, we can plot $s_l(\omega_i)$ for all calculated frequencies, which is so-called the l-th singular values spectrum (SVS). If only the k-th mode dominates in a target system, only one term dominates in Eqn (7) around $\omega\approx\omega_k$. In this case, the frequency, which shows the peak in the first SVS is an estimate of the k-th modal frequency, and the first singular vector $\boldsymbol{u}_1(\omega_k)$ is an estimate of the k-th mode shape of the system:

$$\boldsymbol{\phi}_k=\boldsymbol{u}_1(\omega_k). \tag{9}$$

The modal damping can be estimated from $s_l(\omega)$ around the peak, which is regarded as the piece of the single-degree-of-freedom (SDOF) density function.

3. Consideration of FDD identification

As mentioned in the previous chapter, FDD method is generally applied under the assumption that the input power-spectral matrix is constant ($\boldsymbol{G}_{xx}(\omega)=\boldsymbol{C}$). If this condition does not hold, it is possible to exclude the frequency characteristics when the input is known. However, in most cases, the input characteristics are unknown in the actual field. Here, we will discuss the applicability of the FDD method by reconstructing the theoretical development with impact tests as the target. Furthermore, we will also show the possibility that the modal identification accuracy of the FDD method decreases when the inputs have correlations, even if the input power-spectrum matrix is constant, based on theoretical development focusing on the presence of non-diagonal terms in the input-power spectrum matrix.

3.1. Impact-force case

Equation (10) is the approximation equation in the k-th mode, derived from Eqns (4) and (5). Appendix A presents the detailed derivation process.

$$\boldsymbol{G}_{yy}(j\omega)\approx\sum_{k=1}^{n}\sum_{s=1}^{n}\left\{\frac{\boldsymbol{R}_s^*\boldsymbol{G}_{xx}\boldsymbol{R}_k^T}{(j\omega-\lambda_k)(-\lambda_k-\lambda_s^*)}+\frac{\boldsymbol{R}_k^*\boldsymbol{G}_{xx}\boldsymbol{R}_s^T}{(-j\omega-\lambda_k^*)(-\lambda_k^*-\lambda_s)}\right\}. \tag{10}$$

Considering $\boldsymbol{\gamma}_k$ in Eqn (3) as the k-th modal participation vector, it can be expressed as:

$$\boldsymbol{\gamma}_k=\alpha_k\boldsymbol{\phi}_k^x, \tag{11}$$

where $\boldsymbol{\phi}_k^x$ is the k-th modal vector, the element of which consists of the components subject to input (external force) and α_k is the modal contribution ratio for the k-th mode. Detailed derivations of α_k is provided in Appendix B. The numerator of the first term on the right side in Eqn (10) gives

$$\boldsymbol{R}_s^*\boldsymbol{G}_{xx}\boldsymbol{R}_k^T=\alpha_s^*\alpha_k c_{\bar{s}k}\boldsymbol{\phi}_s^*\boldsymbol{\phi}_k^T, \tag{12}$$

where $c_{\bar{s}k}$ is a scalar:

$$c_{\bar{s}k}=\boldsymbol{\phi}_k^{x*T}\boldsymbol{G}_{xx}\boldsymbol{\phi}_s^x. \tag{13}$$

Similarly, the denominator part gives

$$(j\omega-\lambda_k)(-\lambda_k-\lambda_s^*)=\{\sigma_k-j(\omega-\omega_k)\}(\sigma_{ks}-j\Delta\omega_{dks}), \tag{14}$$

where ω_{dk} is the k-th modal damped circular frequency and

$$\sigma_{ks}=\sigma_k+\sigma_s,\ \Delta\omega_{dks}=\omega_{dk}-\omega_{ds}. \tag{15}$$

Noting that the second term on the right side of Eqn (10) is the complex conjugate and transpose of the first one, substituting Eqns (12) and (14) into Eqn (10) gives Eqn (16):

$$\boldsymbol{G}_{yy}\left|_{\omega\cong\omega_k}\right.\approx\sum_{k=1}^{n}\sum_{s=1}^{n}\left\{s_\omega\left(\omega-\omega_{dk}\right)\alpha_{\bar{s}k}c_{\bar{s}k}\boldsymbol{\phi}_s^*\boldsymbol{\phi}_k^T+\left[s_\omega\left(\omega-\omega_{dk}\right)\alpha_{\bar{s}k}c_{\bar{s}k}\boldsymbol{\phi}_s^*\boldsymbol{\phi}_k^T\right]^H\right\},\tag{16}$$

where

$$s_\omega\left(\omega-\omega_{dk}\right)=\frac{1}{\left\{\sigma_k-j\left(\omega-\omega_{dk}\right)\right\}\left(\sigma_{ks}-j\Delta\omega_{dks}\right)}\tag{17}$$

and

$$\alpha_{\bar{s}k}=\alpha_s^*\alpha_k=\frac{1}{\left(c_s^*+2\lambda_s^*m_s^*\right)\left(c_k+2\lambda_k m_k\right)},\tag{18}$$

where $c_k=\boldsymbol{\phi}_k^T\boldsymbol{C}\boldsymbol{\phi}_k$, $m_k=\boldsymbol{\phi}_k^T\boldsymbol{M}\boldsymbol{\phi}_k$ as the symbols $\boldsymbol{M}$ and $\boldsymbol{C}$ are respectively the mass and viscous damping matrices of the objective system.

Equation (13) can be expressed as:

$$c_{\bar{s}k}=\sum_{l=1}^{N}\sum_{m=1}^{N}\phi_{sl}^*\phi_{km}\left\langle X_l\cdot X_m\right\rangle,\tag{19}$$

where ϕ_{ki} denotes the element of the mode vector ϕ_k and symbol < > shows the ensemble average, namely, $\left\langle X_l\cdot X_m\right\rangle$, the element of matrix $\boldsymbol{G}_{xx}$.

When the inputs are mutually independent, the non-diagonal elements of G_{xx} are zero; hence, Eqn (19) becomes:

$$c_{\bar{s}k}=\sum_{l=1}^{N}\sum_{m=1}^{N}\phi_{sl}^*\phi_{km}\left|X_l\right|^2.\tag{20}$$

Furthermore, when the component l is excited at a node by an impact force X_l in an ideal microtremor system, X_l equals a constant scalar X_c, $c_{\bar{s}k}$ is:

$$c_{\bar{s}k}=\begin{cases}X_c\sum_{m=1}^{N}\phi_{sl}^*\phi_{km} & \left(\text{for microtremor}\right)\\ X_c\sum_{m=1}^{N}\phi_{sl}^*\phi_{km}+X_l\phi_{sl}^*\phi_{kl} & \left(\text{for impact force}\right)\end{cases}.\tag{21}$$

Furthermore, when the orthogonality holds between the modal vectors, Eqn (21) becomes:

$$c_{\bar{s}k}=0\left(k\neq s\right),\ c_{\bar{k}k}=\begin{cases}\tilde{X}_c & \left(\text{for microtremor}\right)\\ \tilde{X}_c+X_l\left|\phi_{kl}\right|^2 & \left(\text{for impact force}\right)\end{cases}.\tag{22}$$

Then the case of $k\neq s$ in Eqn (16) can be omitted, and Eqns (17) and (18), respectively, give:

$$s_\omega\left(\omega-\omega_{dk}\right)=\frac{1}{2\sigma_k\left\{\sigma_k-j\left(\omega-\omega_{dk}\right)\right\}}\quad\left(\because\sigma_{ks}=2\sigma_k,\ \Delta\omega_{dks}=0\right);\tag{23}$$

$$\alpha_{\bar{k}k}=\frac{1}{\left|c_k+2\lambda_k m_k\right|^2}.\tag{24}$$

Substituting Eqns (22) to (23) into Eqn (16), we obtain the output PSD matrix approximation as:

$$\boldsymbol{G}_{yy}\left|_{\omega\cong\omega_k}\right.\approx\sum_{k=1}^{n}d_k\boldsymbol{\phi}_k^*\boldsymbol{\phi}_k^T,$$

$$d_k=\frac{\alpha_{\bar{k}k}c_{\bar{k}k}}{2\sigma_k\left\{\sigma_k-j\left(\omega-\omega_{dk}\right)\right\}}.\tag{25}$$

This approximation equation indicates that the SVS: $s_{kk}\left|_{\omega\cong\omega_k}\right.$ obtained from the FDD identification (Eqn (8)) corresponds to $d_k\left|_{\omega\cong\omega_k}\right.$ for the input case of microtremor and impact force. The difference between the two input cases can be explained using Eqn (22), in other words, an impact force enlarges $c_{\bar{k}k}$ if the k-th mode amplitude at component l (ϕ_{kl}) is not zero. Then the singular value increases significantly only when an impact force is applied to the point (component) with large amplitude in a certain mode.

3.2. Effect of cross-correlation input on identification

It is clear from Eqn (25) that when a target structure is subjected to an impact force and uncorrelated white noises such as ambient vibration, $\boldsymbol{G}_{yy}$ is decomposed by SVD into each mode with high accuracy. Then the first SVS has a clear peak at $\omega=\omega_{dk}$ and the higher-order SVS leads continuously to the first one so that the spectrum shapes a continuous modal-power spectrum for each mode, as illustrated in Figure 1a. It means that the higher-order SVS does not have a peak around $\omega=\omega_{dk}$.

On the other hand, if the target structure is subjected to inputs from the ground or wind force, all the nodes receive strongly correlated inputs. In such cases, the non-diagonal elements of $\boldsymbol{G}_{xx}$ have non-zero values. To investigate its effects on the results of FDD identification, $\boldsymbol{G}_{yy}$ was derived in detail. Although this study only considers the case, in which the two dominant modes are at a given frequency, this is not a loss of generality. Considering the case of k, $s\leq 2$, Eqn (16) gives the below relations which is composed of the four combinations; (k, s) = (1, 1), (1, 2), (2, 1), and (2, 2). This development is similar to the approach of Qu et al. (2018), who discussed the separation of closely spaced modes. Unlike their approach, we discuss the effect of the presence of cross-correlation inputs.

$$\boldsymbol{G}_{yy}\left|_{\omega\cong\omega_k}\right.\approx\sum_{k=1}^{2}\sum_{s=1}^{2}\left\{\boldsymbol{g}_{ks}\left(j\omega\right)+\boldsymbol{g}_{ks}{}^H\left(j\omega\right)\right\},$$

where

$$\boldsymbol{g}_{ks}\left(j\omega\right)=s_{ks}\ \boldsymbol{\phi}_s^*\boldsymbol{\phi}_k^T,\quad s_{ks}=s_\omega\left(\omega-\omega_{dk,s}\right)\alpha_{\bar{s}k}c_{\bar{s}k}.$$

For the case of $k=s$, according to Eqn (23):

$$\boldsymbol{g}_{kk}\left(j\omega\right)+\boldsymbol{g}_{kk}{}^H\left(j\omega\right)=\left\{s_\omega\left(\omega-\omega_{dk,k}\right)+s_\omega\left(\omega-\omega_{dk,k}\right)^H\right\}\alpha_{\bar{k}k}c_{\bar{k}k}\boldsymbol{\phi}_k^*\boldsymbol{\phi}_k^T=\frac{1}{\sigma_k^2+\left(\omega-\omega_{dk}\right)^2}\alpha_{\bar{k}k}c_{\bar{k}k}\boldsymbol{\phi}_k^*\boldsymbol{\phi}_k^T.$$

Then $\boldsymbol{G}_{yy}$ can be represented as Eqn (26):

$$\boldsymbol{G}_{yy}\left|_{\omega\cong\omega_k}\right.\approx\sum_{k=1}^{2}\frac{\alpha_{\bar{k}k}c_{\bar{k}k}}{\sigma_k^2+\left(\omega-\omega_{dk}\right)^2}\boldsymbol{\phi}_k^*\boldsymbol{\phi}_k^T+$$

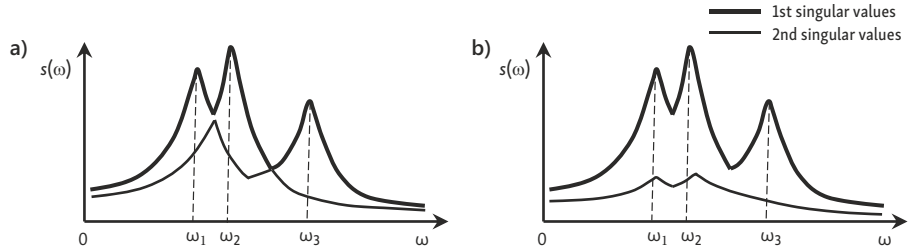

Figure 1. Schematics of: a – non-correlated input case; b – correlated input case of SVS

$$\boldsymbol{g}_{12}(j\omega)+\boldsymbol{g}_{12}^{H}(j\omega)+\boldsymbol{g}_{21}(j\omega)+\boldsymbol{g}_{21}^{H}(j\omega),$$

$$\boldsymbol{g}_{ks}(j\omega)=\frac{\alpha_{sk}c_{\bar{s}k}}{\left(\sigma_k-j\left(\omega-\omega_{dk}\right)\right)\left(\sigma_{ks}-j\Delta\omega_{dks}\right)}\boldsymbol{\phi}_s^{*}\boldsymbol{\phi}_k^{T}. \quad (26)$$

Thus, $\boldsymbol{G}_{yy}$ cannot be perfectly decomposed into the eigenmodes if the inputs are correlated. Then, $\boldsymbol{g}_{ks}$ can be written as:

$$\boldsymbol{g}_{ks}(j\omega)=\frac{1}{\sigma_k^2+\left(\omega-\omega_{dk}\right)^2}\boldsymbol{V}_{ks}, \quad (27)$$

where

$$\boldsymbol{V}_{ks}=\beta_{ks}\zeta_k(\omega)\boldsymbol{\phi}_s^{*}\boldsymbol{\phi}_k^{T}+\left[\beta_{ks}\zeta_k(\omega)\boldsymbol{\phi}_s^{*}\boldsymbol{\phi}_k^{T}\right]^{H}, \quad (28)$$

$$\zeta_k(\omega)=\sigma_k-j\left(\omega-\omega_{dk}\right),$$

$$\beta_{ks}=\alpha_{\bar{s}k}c_{\bar{s}k}\frac{1}{\sigma_{ks}-j\Delta\omega_{dks}}. \quad (29)$$

According to Eqn (28), $\boldsymbol{V}_{ks}$ is a Hermitian matrix; thus, Eqn (30) can be obtained using SVD as:

$$\boldsymbol{g}_{ks}(j\omega)=\frac{1}{\sigma_k^2+\left(\omega-\omega_{dk}\right)^2}\hat{\boldsymbol{V}}_{ks}\hat{\boldsymbol{S}}_{ks}\hat{\boldsymbol{V}}_{ks}^{H}=$$

$$\sum_j\frac{{}_{ks}\hat{s}_j}{\sigma_k^2+\left(\omega-\omega_{dk}\right)^2}{}_{ks}\hat{\boldsymbol{v}}_j\,{}_{ks}\hat{\boldsymbol{v}}_j^{H}, \quad (30)$$

where $\hat{\boldsymbol{S}}_{ks}$ is the singular value matrix consisting of $\hat{s}_j$ and $\hat{\boldsymbol{V}}_{ks}$ is the left singular vector matrix consisting of ${}_{ks}\hat{\boldsymbol{v}}_j$. Using the aforementioned derivations, Eqn (26) gives:

$$\boldsymbol{G}_{yy}\,|_{\omega\equiv\omega_k}\approx\sum_{k=1}^{2}\frac{\alpha_{\bar{k}\bar{k}}c_{\bar{k}\bar{k}}}{\sigma_k^2+\left(\omega-\omega_{dk}\right)^2}\boldsymbol{\phi}_k^{*}\boldsymbol{\phi}_k^{T}+$$

$$\sum_j\frac{{}_{12}\hat{s}_j}{\sigma_1^2+\left(\omega-\omega_{d1}\right)^2}{}_{12}\hat{\boldsymbol{v}}_j\,{}_{12}\hat{\boldsymbol{v}}_j^{H}+$$

$$\sum_j\frac{{}_{21}\hat{s}_j}{\sigma_2^2+\left(\omega-\omega_{d2}\right)^2}{}_{21}\hat{\boldsymbol{v}}_j\,{}_{21}\hat{\boldsymbol{v}}_j^{H}. \quad (31)$$

Equation (31) suggests two conclusions. First, the modal parameters may be identified using the FDD method, even if the inputs are correlated, because the contribution of the first term on the right side is large. However, the accuracy of the modal parameter estimation is expected to be lower because the approximation becomes less accurate in proportion to the strength of the cross-correlation between the inputs. Second, considering the coefficients of the second and third terms in Eqn (31), which respectively take the maximum value around $\omega \cong \omega_{d1}$ and $\omega \cong \omega_{d2}$, a pseudo-peak might be seen in the higher-order SVS at the same peak as the first SVS, as illustrated in Figure 1b. Such a peak should be ignored; however, it is possible the meaningful peak is hidden in the higher-order singular spectrum for the non-correlation input case. Therefore, not only the first, but also the higher-order singular vectors should be checked when several peaks are found around an identified modal frequency.

4. Validation of considerations through numerical experiments

In this chapter, a simple numerical experiment is performed to verify the discussion in the previous chapter. The goal of the verification is both to confirm that the FDD method can accurately identify the natural frequency by peak piking from SVS when an impact force is applied, and to show that the SVS exhibits the characteristics shown in Figure 1b when mutually correlated forces are input, and the identification accuracy is reduced.

Here, a simple 3-DOF model is employed. For this model, four different analysis cases are prepared as shown in Figure 2. Two types of input accelerations are used, one is white noise and the other is the waveform shown in the following equation, which simulates a pseudo-impact (*PI*) force:

$$\ddot{x}_{PI}(t)=\begin{cases}50t & (t\le 0.2s)\\ 0 & (t>0.2s)\end{cases}. \quad (32)$$

In Case 1, different white noises are input to each mass point (Figure 2a). All inputs are uncorrelated each other. In Case 2, pseudo-impact is input to the upper mass (Figure 2b). In Cases 3 and 4, two and three mass are subjected to the same force as Case 2, respectively (Figures 2c and 2d). Different from Cases 1 and 2, the inputs have strongly correlated each other in these two cases. It should be noted that Case 4 is resemble to wind-force input and ground motion input cases, because wind force is often uniform to the structure, and ground motion produces the same inertial force at the mass points.

In the linear response analysis based on Newmark β method (β = 0.25), all the masses and springs were set to 50 ton and 100,000 tf/m, respectively. Rayleigh damping was employed as the viscous damping matrix, using first and second modal damping factors of 3%. Other analytical

conditions for FDD identification are listed in Table 1. In Cases 2 to 4, ensemble averaging was conducted to create the output PSD matrix by shifting the sample wave (Eqn (32)) with 20 time-steps. Response accelerations were used to calculate the output PSD matrix.

Figure 3 shows the singular value spectra for each case obtained using the FDD method, where s_k represents the k-th order singular value. In Case 1, the three singular values are in contact with each other, and each mode power spectrum can be reproduced by connecting the singular values of different orders. This indicates that the three modes could be perfectly decomposed. In Case 2 (Figure 3b), although the first singular value is extremely high because of the contribution of the impact force, and each singular value is separated from the other, the feature shows the same three features as in Figure 3a.

Table 1. Analytical conditions for numerical analysis and FDD for each case

	Case 1	Case 2	Case 3	Case 4
Time increment dt [s]	0.01	0.01	0.01	0.01
Number of data of a sample wave	4096	4096	1024	1024
Number of ensembles	32	128	512	512

On the other hand, in Cases 3 and 4 (Figures 3c and 3d), there are two peaks in the second SVS around the same frequencies as the first SVS, unlike in the other two cases. Equation (31) is only an approximation; however, such peaks can appear if the inputs are correlated.

The eigenfrequencies identified using peak picking (PP) from each first SVS are listed in Table 2, and the corre-

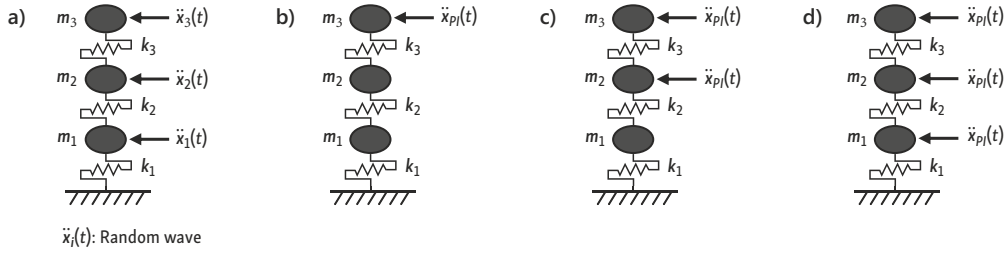

Figure 2. Numerical models: a – Case 1: white noise inputs to all masses (uncorrelated); b – Case 2: pseudo-impact force applied to m_3 (uncorrelated); c – Case 3: pseudo-impact forces applied to m_3 and m_2 (correlated); d – Case 4: pseudo-impact forces applied to all masses (correlated)

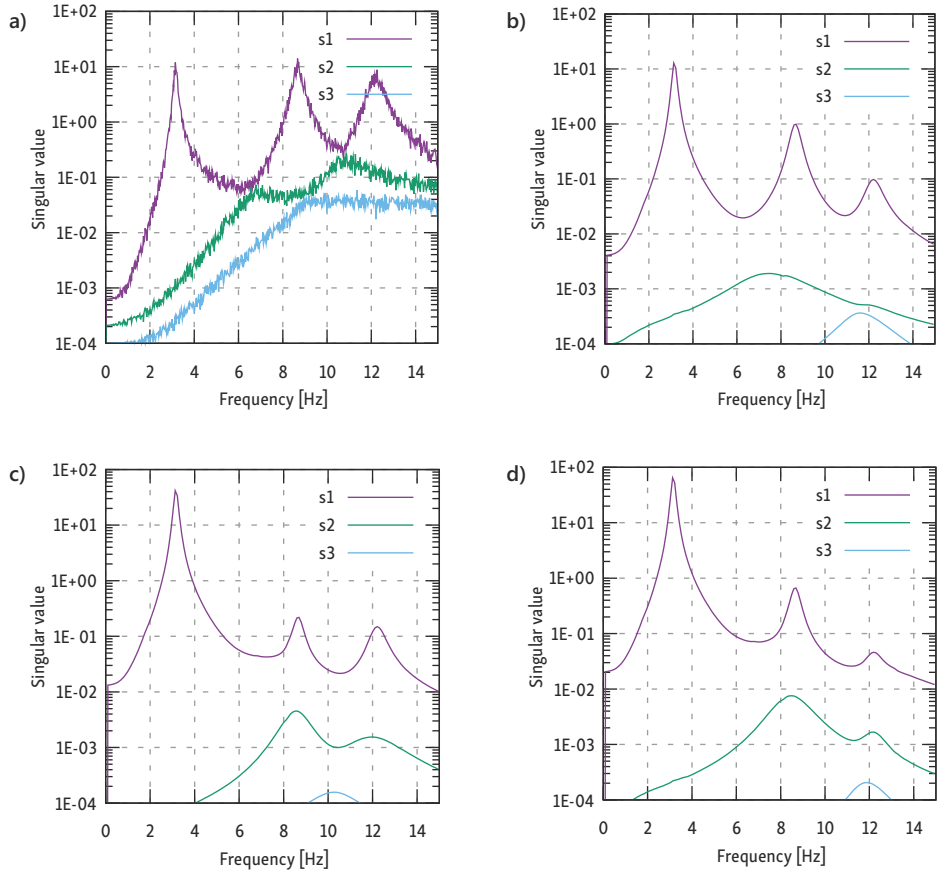

Figure 3. Identified singular value spectra: a – Case 1: white noise inputs to all masses (uncorrelated); b – Case 2: pseudo-impact force applied to m_3 (uncorrelated); c – Case 3: pseudo-impact forces applied to m_3 and m_2 (correlated); d – Case 4: pseudo-impact forces applied to all masses (correlated)

sponding first singular vectors are shown in Figure 4 as the identified mode shapes and their comparison with the theoretical values. According to Table 2 and Figure 4, the eigenfrequencies and corresponding mode shapes appear to be estimated with high accuracy regardless of the case, whereas the third eigenfrequency for Case 4 has an error of around 5% from the theoretical value, and the corresponding mode shape slightly differs from the theoretical mode. These results indicate that the FDD method can be applied to impact the force inputs and can identify the eigenfrequencies and eigenmodes of the correlated inputs.

5. Application to microtremor observation and impact tests

This chapter describes the application of the FDD method to an actual impact-test field not only to verify our considerations but also validate the numerical simulation for pseudo-impact force described in Chapter 4. Field observations were conducted at an under-construction multi-spanned elevated railway bridge. Figure 5 shows a schematic of the entire bridge after the construction was completed, where five observations were made at different construction stages. Among these, we focused on the observation of the one-span bridge, represented as "R2" in Figure 5, owing to its simplicity. Because the adjacent girders "Ct2" and "Ct3" were not completed during the observation period, "R2" was disconnected from the adjacent bridges R1 and R3 at that time. A microtremor observation and three impact tests were conducted. Figure 6 shows the sensor positions and the impact direction in the impact tests.

The microtremor observations were conducted for 20 min per day when the influence of the wind was low, and the impact tests were performed 10 times per position for three different impact positions. Seven velocity sensors were used for the observations, and the data were recorded using 200 Hz sampling. Velocity records for 14

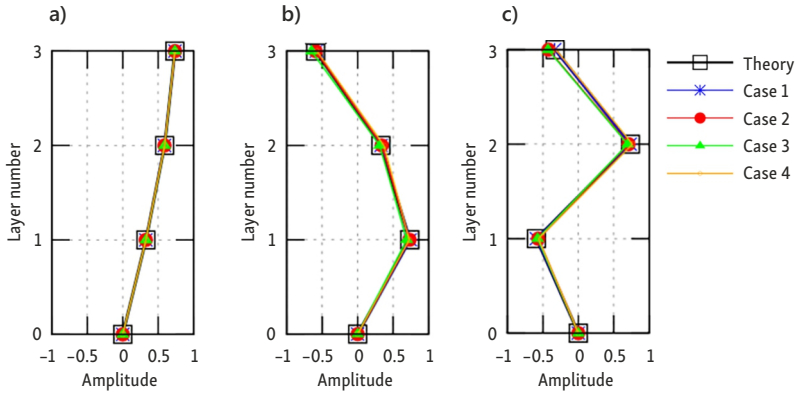

Figure 4. Comparison of mode shapes for each case: a – first mode; b – second mode; c – third mode

Table 2. Comparison of eigenfrequency between theory and each case

Mode order	Theory		Numerical study							
	Freq. [Hz]	Mode amp.	Case 1		Case 2		Case 3		Case 4	
			Freq. [Hz] (Ratio)	MAC	Freq. [Hz] (Ratio)	MAC	Freq. [Hz] (Ratio)	MAC	Freq. [Hz] (Ratio)	MAC
1st	3.168	0.737 0.591 0.327	3.174 (1.002)	1.000	3.149 (0.994)	1.000	3.125 (0.986)	1.000	3.125 (0.986)	1.000
2nd	8.876	0.591 –0.328 –0.737	8.740 (0.976)	1.000	8.642 (0.973)	0.996	8.691 (0.979)	0.940	8.691 (0.979)	0.972
3rd	12.826	0.328 –0.737 0.591	12.231 (0.954)	1.000	12.207 (0.952)	0.954	12.207 (0.952)	0.964	12.207 (0.952)	0.763

Note: *( ) shows the Ratio of the theoretical value.

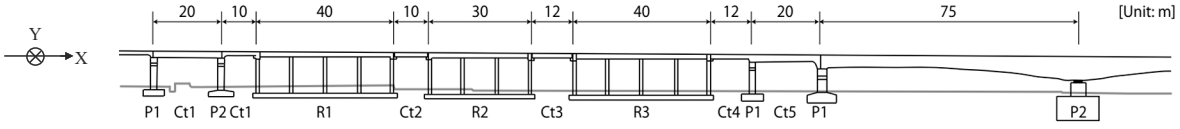

Figure 5. Schematic of the entire target bridge

components (two horizontal components for seven sensors) were used for the FDD analysis. For microtremor observations, 32 portions of 4096 steps with less noise were cut from the records. For the impact tests, the same number of portions was obtained by shifting 50 steps from the free-vibration waveform for a single impact. The 32 waveforms were used as an ensemble average to generate a power spectrum matrix.

We also constructed a simple numerical model of "R2" based on its design document and performed both eigenvalue analysis and numerical response analysis to corroborate the validation using the observed records. The 3D shape of the numerical model and the obtained dominant mode shapes are shown in Figure 7. The first and second modes showed respectively the translational modes for Y- and X-directions. These are clearly the closely-spaced modes. The third one is the tortional mode. Each eigen frequency of the translational modes are close. Using this model, numerical response analyses were performed both for a white-noise input same as Figure 2a and pseudo-impact tests same as Figure 2b. The impact points for the pseudo-impact test are the same as Figure 6.

The SVS identified from response accelerations obtained through numerical analysis are shown in upper of Figure 8. In white-noise input (Figure 8a), all peaks for the three modes are visible along the first SVS (s1) although the second peak is not clear. On the other hand, only one or two peaks are appeared along "s1" for impact input cases (Figures 8b–8d). In these cases, second or third SVS (s2, s3) have peaks instead of s1.

The identified singular vectors are also shown in lower of Figure 8. Here, we showed the vectors correspond not only to s1 but also to s2 and s3 if they have a peak. Each color is identical to SVS, so the red-, green-, and blue-colored vectors (u_1, u_2, and u_3) respectively show the amplitude of the first, second, and third singular vectors. Focusing on the characteristic of u_1 (red-colored mode) in the case of white-noise input, the shapes correspond to the first, second, and third peaks are almost identical to each mode shape of Figure 7. The closely spaced modes

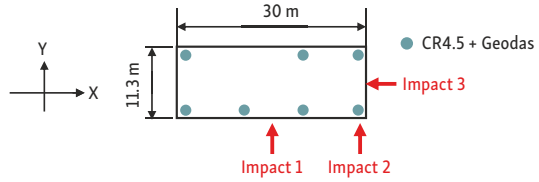

Figure 6. Sensor positions on slab, and impact points and directions of the three impact tests

can be separated to each mode by using MACs for u_1 and u_2 correspond to discretized frequencies around the peak frequency (e.g., Qu et al. 2018). On the other hand, in the case of Impact 1, u_1 at three different peaks show only the translational mode for Y-direction and u_2 and u_3 show the X-direction translational or the tortional modes. Likewise, in Impact 3, all u_1 show only the translational mode for X-direction and u_2 and u_3 show other modes. In the case of impact 2, u_1 is apparently the translational mode for Y-direction for the first and second peaks and is the tortional mode for the third peak. Considering the location and direction of the impact force, these characteristics are reasonable. These results clearly indicate the high-order singular vectors should be focused on when FDD is applied to impact tests.

Similarly, the SVS and singular vectors identified from observation records are shown in Figure 9. Although the peak frequencies and the damping seem to a little different, the outlines of SVS are like those for Figure 8. It indicates the validity of the numerical response simulation to the pseudo-impact force. Based on the observation records, the actual bridge has almost the same frequencies at the first and the second modes. The identified singular vectors are also shown in lower of Figure 9. Different from the numerical study shown in Figure 8, the translational modes seem to be a kind of mixture of Y- and X-translational modes for all the input cases. However, the overall characteristics are accordance with Figure 8. That is, some of eigenfrequencies are often hidden in the second or the third singular values. These results simply demonstrated the importance of the peaks of higher-order singular values.

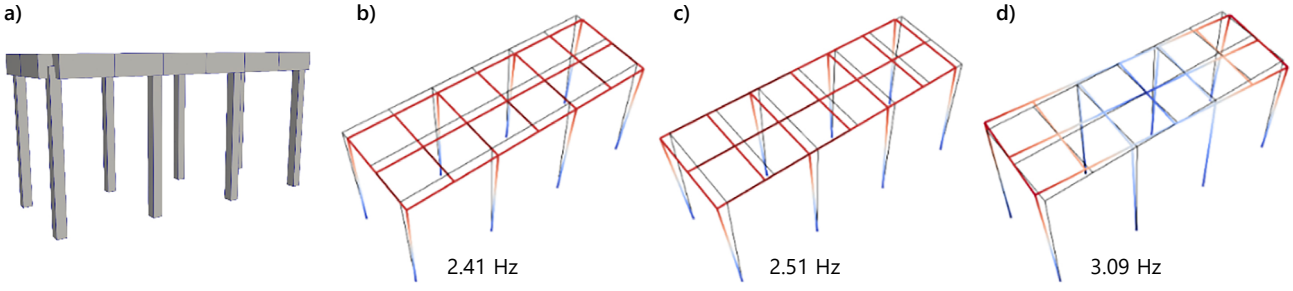

Figure 7. Numerical model of R2 and the mode shapes based on eigenvalue analysis: a – 3D shape of model; b – first mode shape; c – second mode shape; d – third mode shape

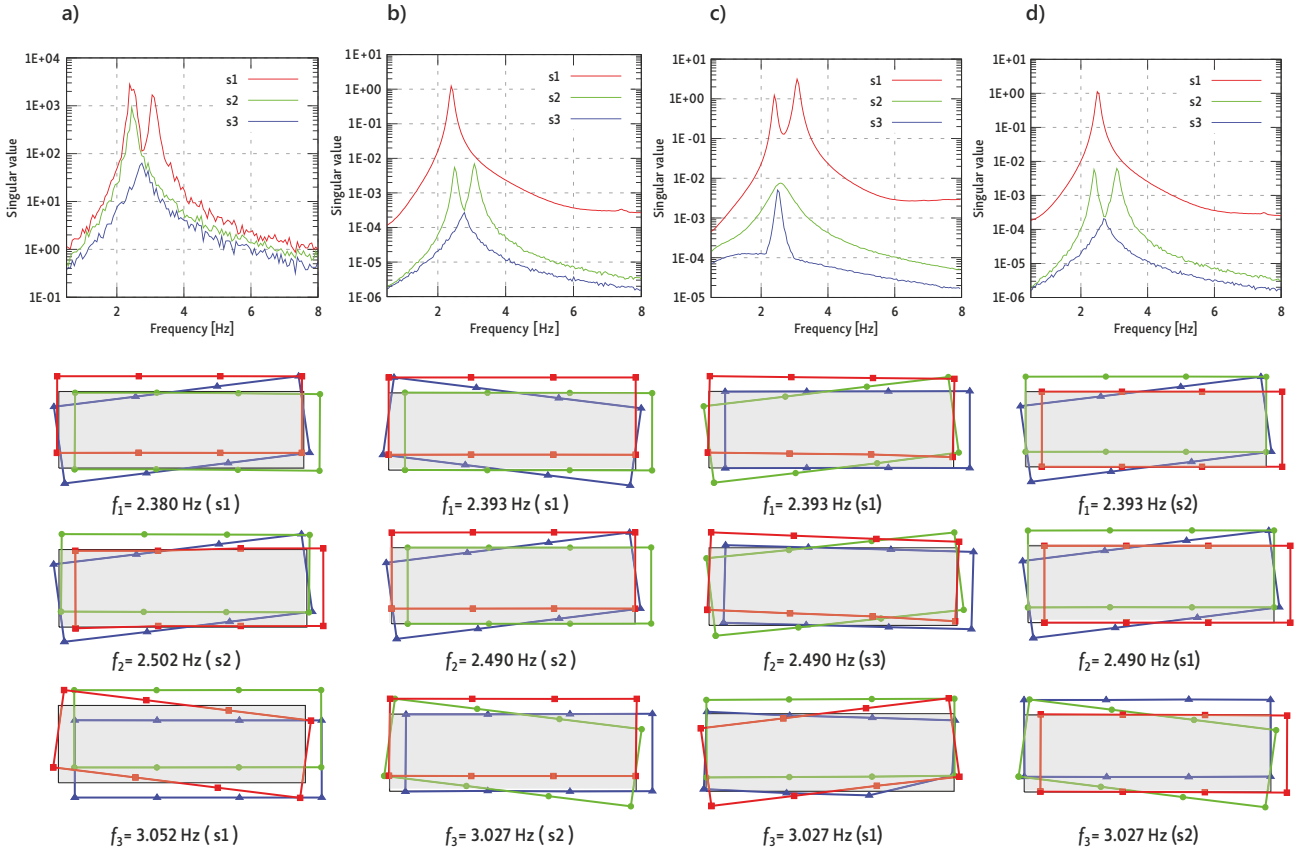

Figure 8. SVS and singular vectors identified from response accelerations obtained through numerical analysis: a – White-noise input (Microtremor-like); b – Impact 1; c – Impact 2; d – Impact 3

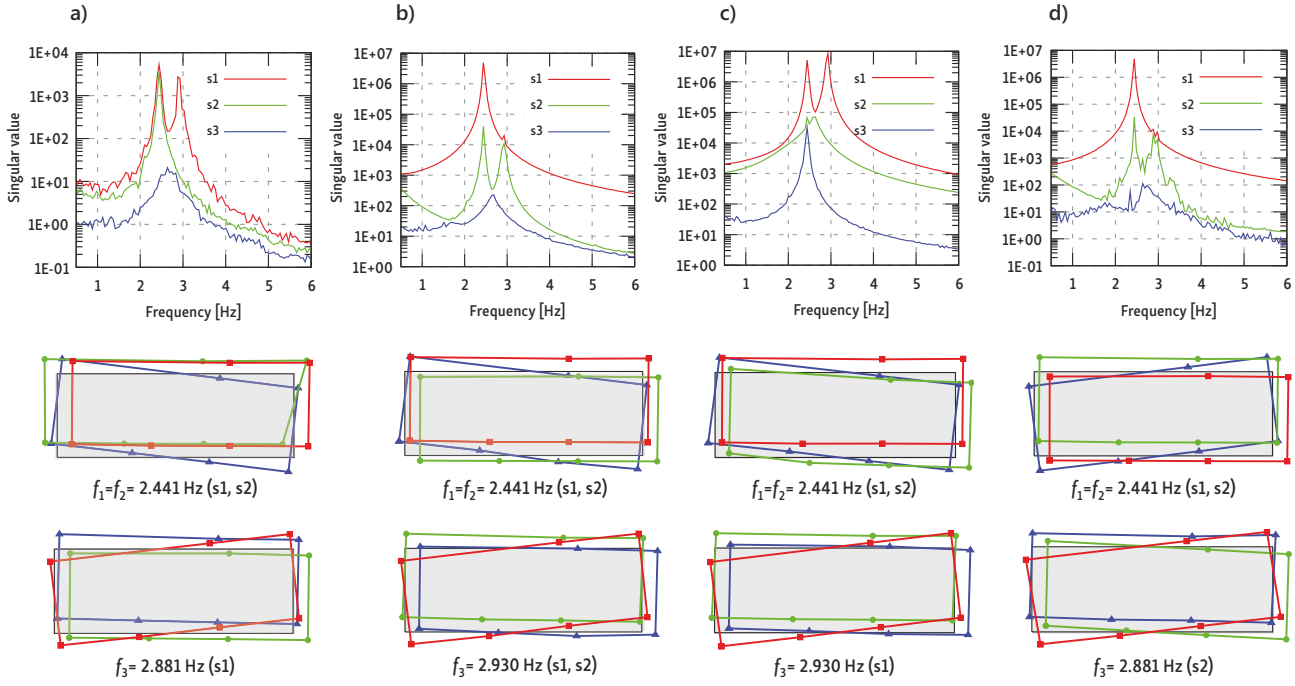

Figure 9. SVS and singular vectors identified from observation records: a – Microtremor; b – Impact 1; c – Impact 2; d – Impact 3

6. Conclusions

In order to clarify the applicability of the FDD method to impact testing, the theoretical background of the original FDD by Brincker et al. (2000) was restructured with a focus on the effects of system inputs. Based on the theoretical development focusing on the characteristics of the power spectrum matrix of the inputs, it was found that the FDD method can be applied to impact tests with good accuracy. Normally, modal identification techniques are used to estimate only the intended modes for impact testing, since the modes are strongly excited depending on the location and direction of the impact force. However, through FDD from microtremor observation and impact test using multiple sensors, clear peaks representing the actual vibration modes appear not only in the peaks based on the first singular value spectrum, but also in the higher singular value spectra. This also suggests the effectiveness of the FDD method, which can focus on higher-order singular values and singular vectors at the same time.

On the other hand, there are cases where the higher-order peaks do not adequately suggest the eigenmode of the targeted system, one of which is the case where the inputs are correlated with each other, as shown in reconstruction of the FDD theory by explicitly representing the effect of the non-diagonal terms of the input-power spectrum matrix. When the system of interest has closely spaced modes, the peaks of the singular values of each order might be close together, and the peaks of the higher order singular values may overlap with the first singular values, in which case the peaks of the higher order singular values may still be visible. This is not a problem in the case of impact testing but considering that the FDD method is affected by weak ground motion and wind during microtremor observations, identification that takes the input conditions into account will be necessary when applying the FDD method to vibration response recordings.

Acknowledgements

We appreciate to Mr. Hikaru Kitamura, Japan Railway Construction, Transport and Technology Agency, for cooperation on the microtremor observation of this research.

Funding

A part of this work was supported by JSPS KAKENHI Grant Number JP19H02400 and LLP Ground Motion Information Laboratory.

Author contributions

Kahori Iiyama conceived of the presented idea. Hitoshi Morikawa helped supervise the project and Kahori Iiyama wrote the manuscript with support from Hitoshi Morikawa. Chen Ping-Yu and Kahori Iiyama carried out the numerical simulations, and Kimitoshi Sakai planned the experiments and provided the target for microtremor observation.

Disclosure statement

The authors have nothing to disclose.

References

Au, S. K. (2011). Fast Bayesian FFT method for ambient modal identification with separated modes. *Journal of Engineering Mechanics*, *137*, 214–226. https://doi.org/10.1061/(ASCE)EM.1943-7889.0000213

Bendat, J. S., & Piersol, A. G. (1993). *Engineering applications of correlation and spectral analysis*. John Wiley & Sons.

Brincker, R., Zhang, L., & Andersen, P. (2000). Output-only modal analysis by frequency domain decomposition. In *Proceedings of ISMA25: 2000 International Conference on Noise and Vibration Engineering* (pp. 717–723), Katholieke Universiteit, Leuven.

Brincker, R., Zhang, L., & Andersen, P. (2001). Modal identification of output-only systems using frequency domain decomposition, *Smart Materials and Structures*, *10*(3), 441–445. https://doi.org/10.1088/0964-1726/10/3/303

Brincker, R., Andersen, P., & Jacobsen, N.-J. (2007). Automated frequency domain decomposition for operational modal analysis. In *Proceedings of IMAC-XXIV: A Conference & Exposition on Structural Dynamics Society for Experimental Mechanics*.

Chen, T., Chen, G., Chen, W., Hou, S., Zheng, Y., & He, H. (2021). Application of decoupled ARMA model to modal identification of linear time-varying system based on the ICA and assumption of "short-time linearly varying". *Journal of Sound and Vibration*, *499*(12), Article 115997. https://doi.org/10.1016/j.jsv.2021.115997

Danial, M., Hasan, A., Ahmad, Z. A. B., Salman, L. M., & Hee, L. M. (2018). Enhanced frequency domain decomposition algorithm: a review of a recent development for unbiased damping ratio estimates. *Journal of Vibroengineering*, *20*(5), 1919–1936. https://doi.org/10.21595/jve.2018.19058

Ermert, L., Poggi, V., Burja'nek, J., & F¨ah, D. (2014): Fundamental and higher two-dimensional resonance modes of an Alpine valley. *Geophysical Journal International*, *198*(2), 795–811. https://doi.org/10.1093/gji/ggu072

Ghannadi, P., & Kourehli, S. S. (2022). Efficiency of the slime mold algorithm for damage detection of large-scale structures. *The Structural Design of Tall and Special Buildings*, 31(14), Article e1967. https://doi.org/10.1002/tal.1967

Ghannadi, P., Khatir, S., Kourehli, S. S., Nguyen, A., Boutchicha, D., & Wahab, M. A. (2023). Finite element model updating and damage identification using semi-rigidly connected frame element and optimization procedure: An experimental validation. *Structures*, *50*, 1173–1190. https://doi.org/10.1016/j.istruc.2023.02.008

Gul, M., & Catbas, F.N. (2011). Structural health monitoring and damage assessment using a novel time series analysis methodology with sensor clustering. *Journal of Sound and Vibration*, *330*, 1196–1210. https://doi.org/10.1016/j.jsv.2010.09.024

Hızal, Ç. (2020). Modified frequency and spatial domain decomposition method based on maximum likelihood estimation. *Engineering Structures*, *224*, Article 111007. https://doi.org/10.1016/j.engstruct.2020.111007

Hızal, Ç. (2023a). FDD based modal identification of structures using least squares approach. *Structures*, *55*, 1071–1083. https://doi.org/10.1016/j.istruc.2023.06.092

Hızal, Ç. (2023b). FRF-based probabilistic modal parameter identification of structures with known seismic input. *Mechanical Systems and Signal Processing*, *189*, Article 110092. https://doi.org/10.1016/j.ymssp.2022.110092

Hızal, Ç., & Aktaş, E. (2021). Probabilistic investigation of error propagation in frequency domain decomposition-based operational modal analysis. *Structural Control and Health Monitoring*, *28*, Article e2759. https://doi.org/10.1002/stc.2759

Hizal, Ç., & Turan, G. (2020). A two-stage Bayesian algorithm for finite element model updating by using ambient response data from multiple measurement setups. *Journal of Sound and Vibration*, *469*, Article 115139. https://doi.org/10.1016/j.jsv.2019.115139

Kang, J., Liu, L., Shao, Y., & Ma, Q. (2021). Non-stationary signal decomposition approach for harmonic responses detection in operational modal analysis. *Computers and Structures*, *242*, Article 106377. https://doi.org/10.1016/j.compstruc.2020.106377

Lee, J. J., & Yun, C. B. (2006). Damage diagnosis of steel girder bridges using ambient vibration data. *Engineering Structures*, *28*, 912–925. https://doi.org/10.1016/j.engstruct.2005.10.017

Mosavi, A. A., Dickey, D., Seracino, R., & Rizkalla, S. (2012). Identifying damage locations under ambient vibrations utilizing vector autoregressive models and Mahalanobis distances. *Mechanical Systems and Signal Processing*, *26*, 254–267. https://doi.org/10.1016/j.ymssp.2011.06.009

Mostafavian, S., Nabavian, S. R., Davoodi, M., & Neya, B. N. (2019). Output-only modal analysis of a beam via frequency domain decomposition method using noisy data. *International Journal of Engineering*, *32*(12), 1753–1761. https://doi.org/10.5829/ije.2019.32.12c.08

Nagamatsu, A. (1993). *Modo kaiseki nyumon* [Introduction to modal analysis]. Corona Publishing Co., Ltd. (in Japanese).

Naira, K. K., Kiremidjianb, A. S., & Law, K. H. (2006). Time series-based damage detection and localization algorithm with application to the ASCE benchmark structure. *Journal of Sound and Vibration*, *291*, 349–368. https://doi.org/10.1016/j.jsv.2005.06.016

Ng, C. T., Wang, P., Au, S. K., & Li, B. (2023). Uncertainty laws of experimental modal analysis with known broadband input. *Mechanical Systems and Signal Processing*, *204*, Article 110624. https://doi.org/10.1016/j.ymssp.2023.110624

Ni, Y. C., & Zhang, F. L. (2019). Fast Bayesian frequency domain modal identification from seismic response data. *Computers and Structures*, *212*, 225–235. https://doi.org/10.1016/j.compstruc.2018.08.018

Noori, M., Rainieri, C., Domaneschi, M., & Sarhosis, V. (Eds.). (2024). *Data driven methods for civil structural health monitoring and resilience. Latest developments and applications*. CRC Press. https://doi.org/10.1201/9781003306924

Pioldi, F., Ferrari R., & Rizzi, E. (2015). Output-only modal dynamic identification of frames by a refined FDD algorithm at seismic input and high damping. *Mechanical Systems and Signal Processing*, *68–69*, 265–291. https://doi.org/10.1016/j.ymssp.2015.07.004

Pioldi, F., Ferrari R., & Rizzi, E. (2017a). Earthquake structural modal estimates of multi-storey frames by a refined frequency domain decomposition algorithm. *Journal of Vibration and Control*, *23*(13), 2037–2063. https://doi.org/10.1177/1077546315608557

Pioldi, F., Salvi, J., & Rizzi, E. (2017b). Refined FDD modal dynamic identification from earthquake responses with soil-structure interaction. *International Journal of Mechanical Science*, *127*, 47–61. https://doi.org/10.1016/j.ijmecsci.2016.10.032

Poggi, V., Ermert, L., Burja'nek, J., Michel, C., & F ¨ah, D. (2014). Modal analysis of 2-D sedimentary basin from frequency domain decomposition of ambient vibration array recordings. *Geophysical Journal International*, *200*(1), 615–626. https://doi.org/10.1093/gji/ggu420

Qin, S., Feng, J., Tang, J., Huo, X., Zhou, Y., Yang, F., & Wahab, M. A. (2024). Condition assessment of a concrete filled steel tube arch bridge using in-situ vibration measurements and an Improved Artificial Fish Swarm Algorithm. *Computers & Structures*, *291*, Article 107213. https://doi.org/10.1016/j.compstruc.2023.107213

Qu, C. X., Yi, T. H., Li, H. N., & Chen, B. (2018). Closely spaced modes identification through modified frequency domain decomposition. *Measurement: Journal of the International Measurement Confederation*, *128*, 388–392. https://doi.org/10.1016/j.measurement.2018.07.006

Qu, C.-X., Liu, Y.-F., Yi, T.-H., & Li, H.-N. (2023). Structural damping ratio identification through iterative frequency domain decomposition. *Journal of Structural Engineering*, *149*(5), Article 04023042. https://doi.org/10.1061/JSENDH.STENG-11837

Rodrigues, J., Brincker, R., & Andersen, P. (2004). Improvement of frequency domain output-only modal identification from the application of the random decrement technique. In *Proceedings of the 23rd International Modal Analysis Conference*, Dearborn, Michigan.

Rodriguez-Suesca, A. E., Gutierrez-Junco, O. J., & Hernandez-Montes, E. (2022). Vibration performance assessment of deteriorating footbridges: A study of Tunja's public footbridges. *Engineering Structures*, *256*, Article 113997. https://doi.org/10.1016/j.engstruct.2022.113997

Suzuki, Y., Iiyama, K., Morikawa, H., Sakai, K., & Araki, G. (2022). New method to estimate bedrock shape of small-scale basin using modal properties of sediment. *Soil Dynamics and Earthquake Engineering*, *149*, Article 106882. https://doi.org/10.1016/j.soildyn.2021.106882

Van, P. N. (2016). Building structure parameter identification using the frequency domain decomposition (FDD) method. In *AETA 2015: Recent Advances in Electrical Engineering and Related Sciences* (pp. 869–880). https://doi.org/10.1007/978-3-319-27247-4_72

Yan, W. J., & Katafygiotis, L. S. (2015). A two-stage fast Bayesian spectral density approach for ambient modal analysis. Part II: Mode shape assembly and case studies. *Mechanical Systems and Signal Processing*, *54*, 156–171. https://doi.org/10.1016/j.ymssp.2014.08.016

Zhang, L., Wang, T., & Tamura, Y. (2005). A Frequency-spatial decomposition (FSDD) technique for operational modal analysis. In *Proceedings of the 1st International Operational Modal Analysis Conference* (*IOMAC*), Copenhagen, Denmark.

Zhang, L., Wang, T., & Tamura, Y. (2010). A frequency–spatial domain decomposition (FSDD) method for operational modal analysis. *Mechanical Systems and Signal Processing*, *24*, 1227–1239. https://doi.org/10.1016/j.ymssp.2009.10.024

APPENDIX

Appendix A

In this study, we have not used the expression $\boldsymbol{G}_{yy}(j\omega) = \boldsymbol{C}$; we introduce a symbol different from the original paper by Brincker et al. Although the derivation of Eqn (10) is traceable, the detailed derivations of Eqns (4) to (31) are explained here. For simplicity, symbols such as "($j\omega$)" and "(ω)" are omitted here. The PSD matrix is:

$$\boldsymbol{G}_{yy} = \boldsymbol{Y}^{*}\boldsymbol{Y}^{T} = \boldsymbol{H}^{*}\boldsymbol{G}_{xx}\boldsymbol{H}^{T}. \tag{A.1}$$

The transfer function of a multi-degree-of-freedom vibration system is represented as

$$\boldsymbol{H} = \sum_{k=1}^{N}\left\{\frac{\boldsymbol{R}_k}{j\omega-\lambda_k}+\frac{\boldsymbol{R}_k^{*}}{j\omega-\lambda_k^{*}}\right\} \tag{A.2}$$

and Eqn (4) can be obtained by substituting Eqn (A.2) into Eqn (A.1):

$$\boldsymbol{G}_{yy} = \sum_{k=1}^{n}\frac{\boldsymbol{A}_k}{j\omega-\lambda_k}+\frac{\boldsymbol{A}_k^{*}}{j\omega-\lambda_k^{*}}+\frac{\boldsymbol{A}_k^{T}}{-j\omega-\lambda_k}+\frac{\boldsymbol{A}_k^{*T}}{-j\omega-\lambda_k^{*}}, \tag{A.3}$$

where A_k is the k-th residue matrix given by the following equation, which is the same as Eqn (5) ($\boldsymbol{G}_{xx}(\omega) = \boldsymbol{\Gamma}$):

$$\boldsymbol{A}_k = \sum_{s=1}^{N}\left\{\frac{\boldsymbol{R}_s}{-\lambda_k-\lambda_s}+\frac{\boldsymbol{R}_s^{*}}{-\lambda_k-\lambda_s^{*}}\right\}\boldsymbol{G}_{xx}\boldsymbol{R}_k^{T}. \tag{A.4}$$

Considering the pole $\lambda_k = -\sigma_k + j\omega_{dk}$, the denominators of Eqn (A.3) give:

$$\begin{aligned}&\pm j\omega-\lambda_k = \sigma_k \pm j\left(\omega\mp\omega_{dk}\right),\\ &\pm j\omega-\lambda_k^{*} = \sigma_k \pm j\left(\omega\pm\omega_{dk}\right).\end{aligned} \tag{A.5}$$

When $\omega \simeq \omega_k$ with the modal damping is small enough $\left(\omega_k \approx \omega_{dk}\right)$, the two terms of Eqn (A.3) including $\omega - \omega_k$ become extremely large and the other two terms become negligible:

$$\boldsymbol{G}_{yy}\,|_{\omega\simeq\omega_{dk}} = \sum_{k=1}^{N}\left\{\frac{\boldsymbol{A}_k}{j\omega-\lambda_k}+\frac{\boldsymbol{A}_k^{*T}}{-j\omega-\lambda_k^{*}}\right\}+o\left(j\omega\right). \tag{A.6}$$

Furthermore, considering

$$\frac{1}{\left|-\lambda_k-\lambda_s\right|} \ll \frac{1}{\left|-\lambda_k-\lambda_s^{*}\right|}, \tag{A.7}$$

the first term of Eqn (A.4) can also be negligible, and A_k can be approximated as:

$$\boldsymbol{A}_k = \sum_{s=1}^{N}\frac{\boldsymbol{R}_s^{*}\boldsymbol{G}_{xx}\boldsymbol{R}_k^{T}}{-\lambda_k-\lambda_s^{*}}+\in\left(j\omega\right). \tag{A.8}$$

Substituting Eqn (A.8), the approximation equation can be obtained as Eqn (A.9), around the k-th mode:

$$\boldsymbol{G}_{yy}\,|_{\omega\simeq\omega_{dk}} \approx \sum_{k=1}^{n}\sum_{s=1}^{n}\left\{\frac{\boldsymbol{R}_s^{*}\boldsymbol{G}_{xx}\boldsymbol{R}_k^{T}}{\left(j\omega-\lambda_k\right)\left(-\lambda_k-\lambda_s^{*}\right)}+\frac{\boldsymbol{R}_k^{*}\boldsymbol{G}_{xx}\boldsymbol{R}_s^{T}}{\left(-j\omega-\lambda_k^{*}\right)\left(-\lambda_k^{*}-\lambda_s\right)}\right\}. \tag{A.9}$$

If $\boldsymbol{G}_{xx} = \boldsymbol{G}_{xx}^{H}$, Eqn (A.9) can be represented as:

$$\boldsymbol{G}_{yy}\,|_{\omega\simeq\omega_{dk}} \approx \sum_{k=1}^{n}\sum_{s=1}^{n}\left\{\frac{\boldsymbol{R}_s^{*}\boldsymbol{G}_{xx}\boldsymbol{R}_k^{T}}{\left(j\omega-\lambda_k\right)\left(-\lambda_k-\lambda_s^{*}\right)}+\left(\frac{\boldsymbol{R}_s^{*}\boldsymbol{G}_{xx}\boldsymbol{R}_k^{T}}{\left(j\omega-\lambda_k\right)\left(-\lambda_k-\lambda_s^{*}\right)}\right)^{H}\right\}. \tag{A.10}$$

Furthermore, Eqn (14) indicates the denominators of the right side of Eqn (A.10) are relatively smaller for $k = s$ than for $k \neq s$, when $\omega \simeq \omega_k$. When $k = s$, Eqn (A.11) is obtained:

$$\left(-\lambda_k-\lambda_k^{*}\right) = 2\sigma_k. \tag{A.11}$$

According to Eqn (12), the numerator of the right side of Eqn (A.10) can be represented as Eqn (A.12), using the symbol $\alpha_{\bar{k}k}$ in Eqn (18):

$$\boldsymbol{R}_k^{*}\boldsymbol{G}_{xx}\boldsymbol{R}_k^{T} = \alpha_{\bar{k}k}c_{\bar{k}k}\boldsymbol{\phi}_k^{*}\boldsymbol{\phi}_k^{T}. \tag{A.12}$$

Just replacing the complex mode with the normal mode $\boldsymbol{\phi}_k^{*}\boldsymbol{\phi}_k^{T} = \boldsymbol{\psi}_k\boldsymbol{\psi}_k^{H}$, Eqn (A.10) becomes:

$$\boldsymbol{G}_{yy}\,|_{\omega\simeq\omega_{dk}} \approx \sum_{k=1}^{n}\left\{\frac{\alpha_{\bar{k}k}c_{\bar{k}k}\boldsymbol{\psi}_k\boldsymbol{\psi}_k^{H}}{2\sigma_k\left(j\omega-\lambda_k\right)}+\left(\frac{\alpha_{\bar{k}k}c_{\bar{k}k}\boldsymbol{\psi}_k\boldsymbol{\psi}_k^{H}}{2\sigma_k\left(j\omega-\lambda_k\right)}\right)^{H}\right\}. \tag{A.13}$$

Rewriting Eqn (7) here:

$$\boldsymbol{G}_{yy}\,|_{\omega\simeq\omega_{dk}} \approx \sum_{k\in Sub(\omega)}\left[\frac{\hat{d}_k\boldsymbol{\phi}_k\boldsymbol{\phi}_k^{H}}{j\omega-\lambda_k}+\left(\frac{\hat{d}_k\boldsymbol{\phi}_k\boldsymbol{\phi}_k^{H}}{j\omega-\lambda_k}\right)^{*}\right].$$

Comparing Eqn (7) with Eqn (A.13), we can obtain the following representation:

$$\hat{d}_k = \frac{\alpha_{\bar{k}k}c_{\bar{k}k}}{2\sigma_k}. \tag{A.14}$$

Appendix B

Although the physical equations for a multi-degree of freedom vibration system have been presented in some references, e.g., the study by Nagamatsu (1993), the process to derivate the transfer function from the basic equation is complex. To clarify the physical meaning of the symbols used in this study, the derivation process is explicitly presented in here.

In a non-proportional damping system subjected to harmonic external force, the equation of motion can be represented as:

$$\boldsymbol{M}\ddot{\boldsymbol{y}}_e + \boldsymbol{C}\dot{\boldsymbol{y}}_e + \boldsymbol{K}\boldsymbol{y}_e = \boldsymbol{X}\left(\omega\right)d\omega e^{j\omega t}, \tag{B.1}$$

where $\boldsymbol{y}_e$ is the relative displacement vector for the harmonic component, and $\boldsymbol{X}\left(\omega\right)d\omega$ is the amplitude of the input for each harmonic component. Introducing $\boldsymbol{z} = \dot{\boldsymbol{y}}$ and rewriting $\boldsymbol{y}_e \to \boldsymbol{y}$ and $\boldsymbol{X}\left(\omega\right) \to \boldsymbol{X}$, Eqn (B.1) can be rewritten as:

$$\boldsymbol{C}\dot{\boldsymbol{y}} + \boldsymbol{M}\dot{\boldsymbol{z}} + \boldsymbol{K}\boldsymbol{y} + \boldsymbol{0}\boldsymbol{z} = \boldsymbol{X}d\omega\cdot e^{j\omega t}. \tag{B.2}$$

Introducing the following trivial formulation, which is given from $\boldsymbol{Mz} = \boldsymbol{M\dot{y}}$,

$$\boldsymbol{M\ddot{y}} + \boldsymbol{0\dot{z}} + \boldsymbol{0y} + \boldsymbol{Mz} = \boldsymbol{0}. \tag{B.3}$$

The common representation can be obtained using $\boldsymbol{w} = \{\boldsymbol{yz}\}^T$:

$$\boldsymbol{D\dot{w}} + \boldsymbol{Ew} = \boldsymbol{F}d\omega \cdot e^{j\omega t}, \tag{B.4}$$

where

$$\boldsymbol{D} = \begin{bmatrix} \boldsymbol{C} & \boldsymbol{M} \\ \boldsymbol{M} & \boldsymbol{0} \end{bmatrix},\ \boldsymbol{E} = \begin{bmatrix} \boldsymbol{K} & \boldsymbol{0} \\ \boldsymbol{0} & -\boldsymbol{M} \end{bmatrix}, \boldsymbol{F} = \begin{Bmatrix} \boldsymbol{X} \\ \boldsymbol{0} \end{Bmatrix}. \tag{B.5}$$

The solution can be defined by $\boldsymbol{w} = \boldsymbol{W}e^{\lambda t}$ without the loss of generality and the solution can be expressed using a coordinate transformation form as:

$$\boldsymbol{w} = \sum_{k=1}^{2N} \eta_k(t)\Psi_k, \tag{B.6}$$

where Ψ_k is the k-th mode vector, $\eta_k(t)$ is the k-th modal displacement whereas $\boldsymbol{w}$ represents the physical displacement. Substituting Eqn (B.6) into Eqn (B.4) and multiplying Ψ^T from left side:

$$\Psi^T\boldsymbol{D}\Psi\dot{\boldsymbol{\eta}} + \Psi^T\boldsymbol{E}\Psi\boldsymbol{\eta} = \Psi^T\boldsymbol{F}d\omega \cdot e^{j\omega t}, \tag{B.7}$$

where

$$\boldsymbol{\eta} = \left[\eta_1(t)\ldots\eta_N(t)\ \eta_{N+1}(t)\ldots\eta_{2N}(t)\right]^T;$$

$$\Psi = \left[\Psi_1 \ldots \Psi_N \ \ \Psi_{N+1} \ldots \Psi_{2N}\right] =$$

$$\begin{bmatrix} \boldsymbol{\phi}_1 \cdots \boldsymbol{\phi}_N & \boldsymbol{\phi}_1^* \cdots \boldsymbol{\phi}_N^* \\ \lambda_1\boldsymbol{\phi}_1 \ldots \lambda_N\boldsymbol{\phi}_N & \lambda_1^*\boldsymbol{\phi}_1^* \ldots \lambda_N^*\boldsymbol{\phi}_N^* \end{bmatrix}.$$

The matrices D and E have the orthogonality and one can describe it as:

$$\Psi^T\boldsymbol{D}\Psi = \begin{bmatrix} \boldsymbol{q} & 0 \\ 0 & \boldsymbol{q}^* \end{bmatrix},\ \boldsymbol{q} = \begin{bmatrix} q_1 & & 0 \\ & \ddots & \\ 0 & & q_N \end{bmatrix},$$

$$\Psi^T\boldsymbol{E}\Psi = \begin{bmatrix} \boldsymbol{e} & 0 \\ 0 & \boldsymbol{e}^* \end{bmatrix},\ \boldsymbol{e} = \begin{bmatrix} e_1 & & 0 \\ & \ddots & \\ 0 & & e_N \end{bmatrix}.$$

Clearly,

$$q_k = c_k + 2\lambda_k m_k. \tag{B.8}$$

Then Eqn (B.7) can be divided into each mode using the orthogonality:

$$\begin{cases} q_k\dot{\eta}_k + e_k\eta_k = \Psi_k^T\boldsymbol{F}d\omega \cdot e^{j\omega t} \\ q_k^*\dot{\eta}_{N+k} + e_k^*\eta_{N+k} = \Psi_k^{*T}\boldsymbol{F}d\omega \cdot e^{j\omega t} \end{cases}. \tag{B.9}$$

Since the lower half of the vector F is zero vector (see Eqn (B.5)), the above equation is the same as:

$$\begin{cases} q_k\dot{\eta}_k + e_k\eta_k = \boldsymbol{\phi}_k^T\boldsymbol{X}d\omega \cdot e^{j\omega t} \\ q_k^*\dot{\eta}_{N+k} + e_k^*\eta_{N+k} = \boldsymbol{\phi}_k^{*T}\boldsymbol{X}d\omega \cdot e^{j\omega t} \end{cases}.$$

When the modal displacement $\dot{\eta}_k = j\omega\eta_k$, the above equation is described as:

$$\left(j\omega q_k + e_k\right)\eta_k = \boldsymbol{\phi}_k^T\boldsymbol{X}d\omega \cdot e^{j\omega t}.$$

Therefore,

$$\eta_k = \frac{\boldsymbol{\phi}_k^T\boldsymbol{X}d\omega \cdot e^{j\omega t}}{j\omega q_k + e_k},\ \eta_{N+k} = \frac{\boldsymbol{\phi}_k^{*T}\boldsymbol{X}d\omega \cdot e^{j\omega t}}{j\omega q_N^* + e_k^*}. \tag{B.10}$$

Substituting Eqn (B.10) into Eqn (B.6) considering $\boldsymbol{w} = \{\boldsymbol{yz}\}^T$, the response can be obtained as the following:

$$\boldsymbol{y} = \sum_{k=1}^{N}\left[\frac{\boldsymbol{\phi}_k^T\boldsymbol{X}}{j\omega q_k + e_k}\phi_k + \frac{\boldsymbol{\phi}_k^{*T}\boldsymbol{X}}{j\omega q_N^* + e_k^*}\phi_k^*\right]d\omega \cdot e^{j\omega t}.$$

Now using the relationships of

$$\lambda_k q d_k = -e_k,\ \lambda_k = -\sigma_k + j\omega_{dk}.$$

The denominators of the right side of Eqn (B.10) are rewritten as:

$$\begin{cases} j\omega q_k + e_k = \sigma_k + j\left(\omega - \omega_{dk}\right)q_k = \left(j\omega - \lambda_k\right)q_k \\ j\omega q_k^* + e_k^* = \sigma_k + j\left(\omega - \omega_{dk}\right)q_k^* = \left(j\omega - \lambda_k^*\right)q_k^* \end{cases}.$$

Then Eqn (B.10) can be described as:

$$\boldsymbol{y} = \sum_{k=1}^{N}\left[\frac{\boldsymbol{\phi}_k^T\boldsymbol{X}/q_k}{j\omega - \lambda_k}\boldsymbol{\phi}_k + \frac{\boldsymbol{\phi}_k^{*T}\boldsymbol{X}/q_k^*}{j\omega - \lambda_k^*}\boldsymbol{\phi}_k^*\right]d\omega \cdot e^{j\omega t}. \tag{B.11}$$

Considering that the matrix part of the numerators of Eqn (B.11) can be described by the commutative expression as:

$$\boldsymbol{\phi}_k^T\boldsymbol{X}\boldsymbol{\phi}_k = \boldsymbol{\phi}_k\boldsymbol{\phi}_k^T\boldsymbol{X}.$$

Thereby Eqn (B.11) gives:

$$\boldsymbol{y} = \sum_{k=1}^{N}\left[\frac{\boldsymbol{\phi}_k^T\boldsymbol{\phi}_k^*/q_k}{j\omega - \lambda_k} + \frac{\boldsymbol{\phi}_k^{*T}\boldsymbol{\phi}_k^*/q_k^*}{j\omega - \lambda_k^*}\right]\boldsymbol{X}d\omega \cdot e^{j\omega t}.$$

Representing the response y in frequency domain, the above can be:

$$\boldsymbol{Y} = \sum_{k=1}^{N}\left[\frac{\boldsymbol{\phi}_k^T\boldsymbol{\phi}_k^*/q_k}{j\omega - \lambda_k} + \frac{\boldsymbol{\phi}_k^{*T}\boldsymbol{\phi}_k^*/q_k^*}{j\omega - \lambda_k^*}\right]\boldsymbol{X}.$$

Therefore, the transfer function is given as Eqn (B.12):

$$\boldsymbol{H} = \sum_{k=1}^{N}\left\{\frac{\boldsymbol{\phi}_k\boldsymbol{\phi}_k^T/q_k}{j\omega - \lambda_k} + \frac{\boldsymbol{\phi}_k^*\boldsymbol{\phi}_k^{*T}/q_k^*}{j\omega - \lambda_k^*}\right\}. \tag{B.12}$$

Introducing the scalar α_k as:

$$\alpha_k = \frac{1}{q_k}, \tag{B.13}$$

Eqn (B.12) is given by Eqn (B.14).

$$\boldsymbol{H} = \sum_{k=1}^{N}\left\{\frac{\alpha_k\boldsymbol{\phi}_k\boldsymbol{\phi}_k^T}{j\omega - \lambda_k} + \frac{\alpha_k^*\boldsymbol{\phi}_k^*\boldsymbol{\phi}_k^{*T}}{j\omega - \lambda_k^*}\right\}. \tag{B.14}$$

Equation (2) is rewritten here,

$$\boldsymbol{H} = \sum_{k=1}^{N}\left\{\frac{\boldsymbol{R}_k}{j\omega - \lambda_k} + \frac{\boldsymbol{R}_k}{j\omega - \lambda_k^*}\right\}, \tag{2}$$

and comparing Eqn (B.13) with Eqn (2), the following equation holds, which is shown in Eqns (3) and (11):

$$\boldsymbol{R}_k = \alpha_k\boldsymbol{\phi}_k\boldsymbol{\phi}_k^T = \boldsymbol{\phi}_k\left(\alpha_k\boldsymbol{\phi}_k^T\right) = \boldsymbol{\phi}_k\boldsymbol{\gamma}_k^T.$$

From Eqns (B.8) and (B.13):

$$\alpha_k = \frac{1}{c_k + 2\lambda_k m_k}. \tag{B.12}$$

Therefore $\alpha_{\overline{sk}}$ can be given by Eqn (18).

$$\alpha_{\overline{sk}} = \alpha_s^*\alpha_k = \frac{1}{\left(c_s^* + 2\lambda_s^* m_s^*\right)\left(c_k + 2\lambda_k m_k\right)}. \tag{18}$$